JOURNAL OF THERMOPHYSICS AND HEAT TRANSFER
Vol. 17, No. 1, January–March 2003

Variable Property Nusselt Numbers in a Channel with Pin Fins

Phillip M. Ligrani* and Gazi I. Mahmood†
University of Utah, Salt Lake City, Utah 84112-9208

Nusselt numbers and friction factors are presented that show the effects of temperature ratio and variable properties in a rectangular channel with pin fins and an aspect ratio of 8. The ratio of air inlet stagnation temperature to local surface temperature T_{0i}/T_w varies from 0.68 to 0.93, and Reynolds numbers based on channel height range from 1.8×10^4 to 3.38×10^4. The pins are placed in 12 rows, with pin diameter and spacing between adjacent pins in both directions all equal to the channel height. Ratios of globally averaged Nusselt numbers to baseline, constant-property Nusselt numbers, $\overline{Nu}/\overline{Nu}_{0,\mathrm{cp}}$, increase by about 35% as the temperature ratio T_{0i}/T_w decreases, provided that Reynolds number Re_H is approximately constant and that the base areas beneath the pins are not considered. When heat transfer from the pin fins is also included, this increase is about the same. Friction factor ratios $f/f_{0,\mathrm{cp}}$ decrease as T_{0i}/T_w decreases over this same range of values. Such global Nusselt number changes are a result of local Nusselt number ratio increases with decreasing temperature ratio, which are especially pronounced beneath the wake and shear layers that are present downstream of each pin and beneath the horseshoe vortex that forms just upstream of each pin fin.

Nomenclature

D_h	=	channel hydraulic diameter
d	=	pin fin diameter
f	=	friction factor
f_0	=	baseline friction factor in a smooth channel with no pin fins
H	=	channel height
k	=	thermal conductivity
Nu	=	local Nusselt number, $\dot{q}_0'' D_h/k(T_w - T_{\mathrm{mx}})$
Nu_0	=	baseline Nusselt number in a smooth channel with no pin fins
Pr	=	molecular Prandtl number
p	=	streamwise spacing of pin fin centers
p'	=	streamwise spacing between adjacent pin fins
$\dot{q}_0''$	=	surface heat flux
Re_{Dh}	=	Reynolds number based on hydraulic diameter and mean velocity at test section inlet
Re_d	=	Reynolds number based on pin fin diameter and mean velocity at minimum flow area
Re_H	=	Reynolds number based on channel height and mean velocity at test section inlet
s	=	spanwise spacing of pin fin centers
s'	=	spanwise spacing between adjacent pin fins
T	=	local static temperature
W	=	channel width
X	=	streamwise coordinate measured from the test section inlet
Z	=	spanwise coordinate measured from the test surface centerline

Subscripts

cp	=	constant property value
mx	=	local mixed-mean value
0	=	baseline value
0i	=	total or stagnation value at the test section inlet
w	=	local wall value

Superscripts

–	=	value spatially averaged along a line either in the streamwise or spanwise direction
=	=	globally averaged value

I. Introduction

SHORT pin fins, with length-to-diameter ratios of about one or less, which extend the entire width between two opposite walls of channels, are used for internal cooling of a variety of devices, such as gas-turbine airfoils, combustion chamber liners, compact heat exchangers, and electronic devices. Many existing studies consider the influences of the pin geometry, pin materials, pin-fin array configuration, channel geometry, and different Reynolds numbers. Of the earlier investigations, Zukauskas,[1] Sparrow et al.,[2] Metzger and Haley,[3] and Metzger et al.[4] report Nusselt numbers on flat surfaces, as well as on pin surfaces, and indicate the presence of large overall heat transfer augmentations for certain flow conditions and pin-fin array arrangements. Van Fossen[5] presents heat transfer coefficients measured on circular pin fins made of different materials, which are placed in rectangular cross section channels. Different end-wall plate-to-air temperature differences are employed. The Reynolds number dependence of the results is described, along with comparisons with available correlations for constant-property conditions. Brigham and Van Fossen[6] report large overall heat transfer and mass transfer augmentations for circular pin fins arranged in in-line and staggered arrays. In another study, Simoneau and Van Fossen[7] measure pin surface heat transfer coefficients and streamwise turbulence intensities as the test section gas temperature varies between 260 and 290 K. The authors describe the effects of changing the number of pin rows, without any mention of the influences of the ratio of surface temperature to gas temperature.

Later investigations by Lau et al.[8] and McMillin and Lau[9] consider the effects of bleed ejection on heat and mass transfer distributions and on streamwise pressure variations in a channel with circular pin fins. Chyu,[10] Chyu and Goldstein,[11] and Chyu et al.[12] measure surface mass transfer coefficients using naphthalene-sublimation measurement techniques. Local and spatially averaged mass transfer coefficients are reported for different

Received 8 April 2002; revision received 29 July 2002; accepted for publication 30 July 2002.

*Professor, Convective Heat Transfer Laboratory, Department of Mechanical Engineering, MEB 2202, 50 South Central Campus Drive.

†Postdoctoral Research Fellow, Department of Mechanical Engineering; currently Postdoctoral Research Fellow, Department of Mechanical Engineering, Louisiana State University, Baton Rouge, LA 70803.

pin-fin arrays that provide evidence of large overall mass transfer augmentations for certain in-line and staggered circular arrays. Grannis and Sparrow[13] numerically simulate the two-dimensional flow and pressure fields around diamond-shaped pin fins. Olson[14] describes the behavior of helium flowing through a channel with pins at different wall-to-fluid temperature differences. Presented are normalized pressure drop and wall Nusselt number data as dependent on Reynolds number and wall heat flux magnitude. The investigators employ a temperature ratio/power law scheme to account for variations of thermophysical properties on measured Nusselt numbers. Chyu,[10] Grannis and Sparrow,[13] Goldstein et al.,[15] Chyu and Natarajan,[16] Chyu et al.,[17] Hwang and Lu,[18] and Uzol and Camci[19,20] consider the effects of different pin-fin shapes on heat transfer and flow in internal passages. A variety of pin-fin shapes are considered, including circular,[10,15–20] pins with end-wall fillets,[10] diamond,[13,16] three-dimensional protruding elements,[16] cubic,[16,17] and elliptical.[19,20] Of these studies, the one described by Hwang and Lu[18] is especially unique because three pin-fin configurations, each arranged in a staggered array, are considered in a trapezoidal duct, both with and without lateral flow ejection.

Even though these studies provide much information on pin-fin performance in constant-property flows, almost no information is given on the influences of temperature ratio and variable properties on Nusselt numbers and friction coefficients in internal passages with pin fins. Such variable property effects are present when absolute viscosity, molecular thermal conductivity, specific heat, or static density change with channel location because of variations of the local static temperature. These effects generally become important when the ratio of inlet stagnation temperature to local surface temperature, T_{0i}/T_w, is less than about 0.9 and can alter heat transfer and pressure losses in internal flow ducts (without augmentation devices) by significant amounts.[21] The present paper addresses this issue by presenting a number of time-averaged quantities, including spatially resolved Nusselt numbers, spatially averaged Nusselt numbers, globally averaged friction factors, and globally averaged thermal performance parameters for the bottom test surface of a pin-fin channel at different ratios of inlet stagnation temperature to local surface temperature, T_{0i}/T_w. These results provide information on the influences of variable properties of air for a situation where the gas is heated by the walls of the channel. The measurements are given for a channel aspect ratio of eight, temperature ratios from 0.68 to 0.93, and Reynolds numbers Re_H from 1.8×10^4 to 3.38×10^4. The pins are placed in 12 rows with pin diameter and spacing between adjacent pins in both directions, all equal to the channel height. The ratio of centerline pin-fin spacing to channel hydraulic diameter is 1.12.

II. Experimental Apparatus and Procedures

The overall experimental apparatus (but not the test section) is similar to the one described by Mahmood et al.[22] A brief description of this apparatus is also presented here.

A. Channel and Test Surface for Heat Transfer Measurements

A schematic of the facility used for heat transfer measurements is shown in Fig. 1. The air used within the facility is circulated in a closed loop. One of two circuits is employed, depending on the Reynolds number and flow rate requirements in the test section. The loop with a 102-mm pipe is connected to the intakes of an ILG Industries 10P type blower and a Dayton 7C447 1.0 hp blower and is used for Re_H less than 3.5×10^4. For higher Reynolds number Re_H requirements, the loop with the 203-mm pipe and a 7.5-hp centrifugal blower is used. In each case, the air mass flow rate from the test section is measured (upstream of whichever blower is employed) using an American Society of Mechanical Engineers (ASME) standard orifice plate and Validyne M10 digital pressure manometer. The blower then exits into a series of two plenums (0.9 and 0.75 m square). A Bonneville crossflow heat exchanger is located between two of these plenums and is cooled with liquid nitrogen at flow rate appropriate to give the desired air temperature at the exit of the heat exchanger. As the air exits the heat exchanger, it enters the second plenum, from which the air passes into a rectangular

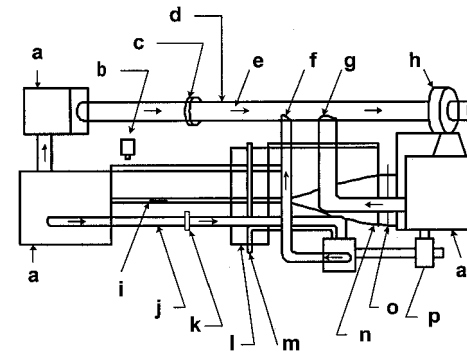

Fig. 1 Schematic diagram of the experimental apparatus used for heat transfer and static pressure measurements: a, plenum; b, infrared camera; c, large orifice plate; d, large blower return duct; e, arrows show flow direction; f, large blower bleed air return; g, large blower by-pass; h, large blower; i, test section; j, small blower return duct; k, small orifice plate; l, boundary layer bleed-off plenum; m, bleed air return; n, inlet nozzle; o, flow straighteners; and p, small blower.

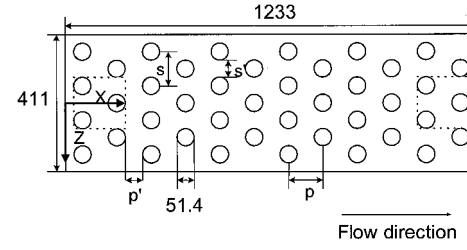

Fig. 2 Schematic diagram of the pin-fin test section, including coordinate system and dimensions; all dimensions are given in millimeters: $s = 102.7$, $s' = 51.4$, $p = 102.7$, and $p' = 51.4$.

bell mouth inlet, followed by a honeycomb, two screens, and a two-dimensional nozzle with a contraction ratio of 11.2. This nozzle leads to a rectangular cross section, 411×51.5 mm inlet duct that is 1219 mm in length. This is equivalent to 13.3 hydraulic diameters (where hydraulic diameter is 91.5 mm). Two trips are employed on the top and bottom surfaces of the inlet duct, just upstream of the test section, which follows with the same cross-section dimensions and an aspect ratio of 8. The test section exits to a 0.60-m square plenum, which is followed by two pipes, each containing an orifice plate, as mentioned earlier.

Figure 2 shows the geometric details of the test surface, including pin-fin geometry and the coordinate system employed for the measurements. A total of 42 short cylindrical pins with uniform diameter and diameter-to-height ratio of one are used in the test section. Thus, the pins extended from the channel bottom wall to the top wall and are arranged in a staggered array with 12 rows in streamwise direction, with three to four pins in each row. The ratio of the pin pitch to channel hydraulic diameter in both the streamwise and spanwise directions is the same, equal to 1.12. The top wall of the test section has two cut-out regions (one at the upstream end and one at the downstream end) where a zinc–selenide window can be installed to allow the infrared camera to view a portion of the bottom wall test surface. The pin fins and the channel walls are made of the same acrylic material. The thickness of the top and bottom acrylic test surfaces is 3.2 mm. With this arrangement, and because of the low thermal conductivity of acrylic ($k = 0.16$ W/m · K at 20 °C), conduction in the streamwise and spanwise directions is minimized along the test surfaces.

All exterior surfaces of the facility (between the heat exchanger and test section) are insulated with Styrofoam ($k = 0.024$ W/m · K), or two to three layers of 2.54-cm-thick Elastomer Products black neoprene foam insulation ($k = 0.038$ W/m · K) to minimize heat losses. Calibrated copper–constantan thermocouples are located between the three layers of insulation located all around the test section to determine conduction losses. Between the first layer and the 3.2-mm-thick acrylic test surfaces are custom-made Electrofilm etched-foil heaters (each encapsulated between two thin layers of Kapton®),

which are placed on all four channel walls. A total of five of these heaters are employed, one for each wall of the channel and one for the insert that is used in the upstream cutout region on the top wall (when the zinc–selenide window is not installed at this location). These provide a constant heat flux boundary condition on the side of the 3.2-mm-thick acrylic surfaces that is located away from the airstream. The power to each of the foil heaters is controlled and regulated using a separate variac power supply. Energy balances, performed on the heated test surface, are then used to determine local magnitudes of the convective heat flux. These energy balances account for conduction losses through the insulation and Styrofoam located behind each test surface. No corrections for conduction along the test surfaces are employed to account for small variations of heat flux that may occur in the acrylic next to the airstream (near to each pin fin). However, possible errors due to such conduction are included in uncertainty estimates for measured local Nusselt number ratios.

The acrylic surfaces, which are adjacent to the airstream, contain 34 copper–constantan thermocouples, which are placed within the pins, within the flat portions of the test surface between the pins, and in the smooth sidewalls. Each of these thermocouples is located 0.051 cm just below the flat parts of the test surfaces to provide measurements of local surface temperatures, after correction for thermal contact resistance and temperature drop through the 0.051-cm thickness of acrylic.

B. Local Nusselt Number Measurements

The mixed-mean stagnation temperature of the air entering the test section is measured using five calibrated copper–constantan thermocouples spread across the inlet cross section. To determine this temperature, thermocouple-measured temperatures are corrected for thermocouple wire conduction losses, channel velocity variations, as well as for the differences between stagnation and recovery temperature. Magnitudes of the local mixed mean temperatures at different locations though the test section T_{mx} are subsequently determined using energy balances and the mixed mean temperature at the inlet of the test section. Because of the way in which it is measured, this inlet stagnation temperature T_{0i} is also a mixed mean value and, thus, is determined over the cross-sectional area of the test section inlet. The thermal conductivity k used to determine local Nusselt numbers is based on this inlet stagnation temperature T_{0i}. All measurements used to determine such Nusselt numbers are obtained when the test facility at steady state.

To determine the surface heat flux (used to calculate heat transfer coefficients and local Nusselt numbers), the total convective power level, provided by each etched-foil heater, is divided by the flat test surface area of that foil heater. Spatially resolved temperature distributions along the bottom test surface are determined using infrared imaging in conjunction with thermocouples, energy balances, and in situ calibration procedures.[22,23] To accomplish this, the infrared radiation emitted by the heated interior surface of the channel is captured using a VideoTherm 340 infrared imaging camera, which operates at infrared wavelengths from 8 to 14 μm. Test surface temperatures are measured using the calibrated, copper–constantan thermocouples distributed along the surface adjacent to the flow, mentioned earlier. These are used to perform the in situ calibrations simultaneously as images from the infrared camera are recorded.

This is accomplished as the camera views the test surface through a custom-made, zinc–selenide window (which transmits infrared wavelengths between 6 and 17 μm) as mentioned earlier. There are 11–12 thermocouple junction locations usually present in the infrared field viewed by the camera. The exact spatial locations and pixel locations of these thermocouple junctions and the coordinates of a 12.7×12.7 cm field of view are known from calibration maps obtained before measurements.

Images from the infrared camera are recorded as 8-bit grayscale images on commercial videotape using a Panasonic AG-1960 video recorder. Images are subsequently digitized using NIH Image version 1.60 software, operated on a Power Macintosh 7500 PC computer. Subsequent software is used to convert each of 256 possible grayscale values to local Nusselt number values at each pixel location using calibration data. Each individual image covers a 300×300 pixel area. Voltages from the thermocouples (used for measurement of air temperatures and in situ calibration of infrared images) are acquired using Hewlett–Packard 44422T data acquisition cards installed in a Hewlett–Packard 3497A data acquisition control unit, which is controlled by a Hewlett–Packard A4190A Series computer. Mahmood et al.[22] and Sargent et al.[23] provide additional details on the infrared imaging and measurement procedures.

C. Friction Factor Measurements

Wall static pressures are measured along the test section simultaneously as the heat transfer measurements are conducted, using 12 static pressure taps, located 25.4–80 mm apart along one of the test section side walls. These measurements are made in the test section with the pin fins, as well as in a baseline test section with smooth surfaces on all four walls. Friction factors are subsequently determined from streamwise pressure gradient magnitudes. Pressures from the wall pressure taps are measured using Celesco LCVR pressure transducers. Signals from these transducers are processed using Celesco CD10D carrier demodulators. Voltages from the carrier demodulators are acquired using a Hewlett–Packard 44422A data acquisition card installed in a Hewlett–Packard 3497A data acquisition control unit, which is controlled by a Hewlett–Packard A4190A Series computer. With this apparatus, 100 sequential measurements are acquired and measured from each pressure transducer, over a time period of about 20 s.

D. Experimental Uncertainty Estimates

Uncertainty estimates are based on 95% confidence levels and determined using procedures described by Kline and McClintock[24] and Moffat.[25] Uncertainty of temperatures measured with thermocouples is 0.15°C. Spatial and temperature resolutions achieved with the infrared imaging are about 0.52 mm and 0.8°C, respectively. This magnitude of temperature resolution is due to uncertainty in determining the exact locations of thermocouples with respect to pixel values used for the in situ calibrations. Local Nusselt number ratio uncertainty is then about ± 0.16 (for a ratio of 2.00), or about $\pm 8.0\%$. Reynolds number uncertainty is approximately $\pm 1.7\%$ for $Re_H = 1 \times 10^4$. The uncertainty for friction factor ratios is about $\pm 8.0\%$.

III. Experimental Results and Discussion

In the discussion that follows, constant property refers to Nusselt numbers measured when T_{0i}/T_w is approximately 1.0 and density, specific heat, viscosity, and thermal conductivity are approximately constant throughout the flow in the channel. Variable property refers to Nusselt numbers measured when significant variations of these properties are present, which occurs as T_{0i}/T_w becomes less than about 0.9. Included in the discussions are comparisons with variable-property results and constant-property results from internal passages from other studies.[21,22,26–29]

A. Baseline Nusselt Numbers

Both variable-property and constant-property baseline Nusselt numbers are measured in a smooth rectangular test section with smooth walls on all surfaces and no pin fins. Except for the absence of the pins and a different aspect ratio, all geometric characteristics of the channel are the same as when the pin-fin test surfaces are installed. The baseline measurements are made in the downstream portion of the test section, where the channel flow is hydraulically and thermally fully developed. Average values are presented that are determined from measurements made on the top and bottom walls. Baseline Nu_0 values are also time averaged and obtained with a constant heat flux boundary condition around the entire test section, that is, on all four channel walls, which is the same type of thermal boundary condition that is utilized when pin fins are used in the channel.

The variations of the constant-property baseline Nusselt numbers $Nu_{0,\mathrm{cp}}$ with Reynolds number Re_{Dh} are shown in Fig. 3 for $T_{0i}/T_w = 0.93$–0.94. The values in Fig. 3 are in agreement with the

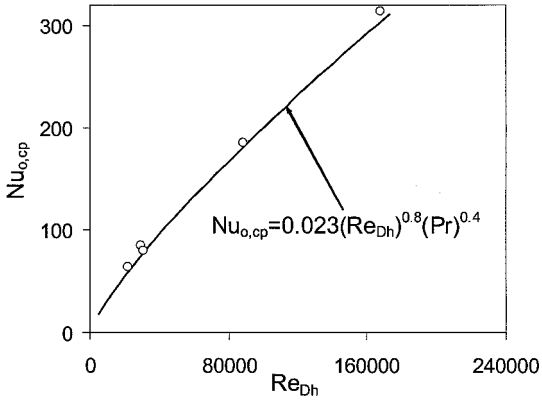

Fig. 3 Baseline, constant-property Nusselt numbers, measured with smooth channel surfaces and constant heat flux boundary condition on all channel surfaces for $T_{0i}/T_w = 0.92$–0.94, as dependent on Reynolds number based on hydraulic diameter, Re_{Dh}.

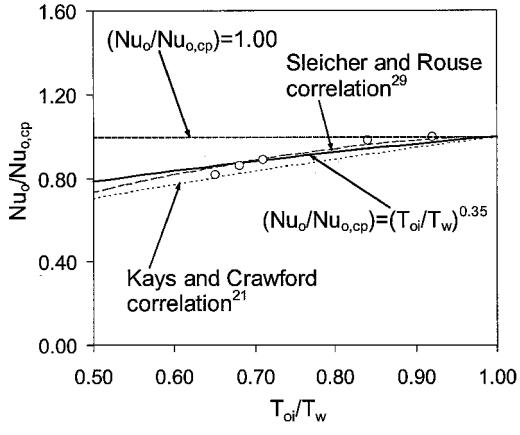

Fig. 4 Baseline, variable-property Nusselt number ratios in a smooth channel, measured with a constant heat flux boundary condition on all channel surfaces, as dependent on temperature ratio T_{0i}/T_w.

Colburn smooth circular tube correlation (see Ref. 26) for the entire range of Reynolds numbers Re_{Dh} shown. These constant-property baseline Nusselt numbers $Nu_{0,cp}$ are employed in the next section to normalize pin-fin channel Nusselt numbers.

Figure 4 gives variable-property baseline Nusselt number Nu_0 data (which are also spatially averaged), as dependent on the ratio of inlet stagnation temperature to local surface temperature T_{0i}/T_w, where values of this parameter are as low as 0.66. Here, Reynolds number Re_{Dh} is approximately constant for these measurements and ranges from 2.61×10^4 to 3.4×10^4. The data are normalized by the constant-property baseline Nusselt number $Nu_{0,cp}$, which is determined at $T_{0i}/T_w = 1.0$ and $Re_{Dh} = 3.0 \times 10^4$. The present data are well represented by an equation given by

$$Nu_0/Nu_{0,cp} = (T_{0i}/T_w)^n \tag{1}$$

where $n = 0.35$. Figure 4 also shows $Nu_0/Nu_{0,cp}$ variations based on two correlations given by Kays and Crawford[21] and Sleicher and Rouse[29] for variable property effects of turbulent gas flows in circular tubes with heating. Values of n for these correlations are 0.5, and approximately 0.4, respectively, which give Nusselt number Nu_0 values that decrease relative to $Nu_{0,cp}$ as T_{0i}/T_w decreases. The present $Nu_0/Nu_{0,cp}$ results, correlated using Eq. (1), are then qualitatively consistent with the correlations from these two sources because they also decrease as T_{0i}/T_w decreases. When uncertainty intervals are considered, the present data are also in agreement with the correlations from these two other sources.[21,29]

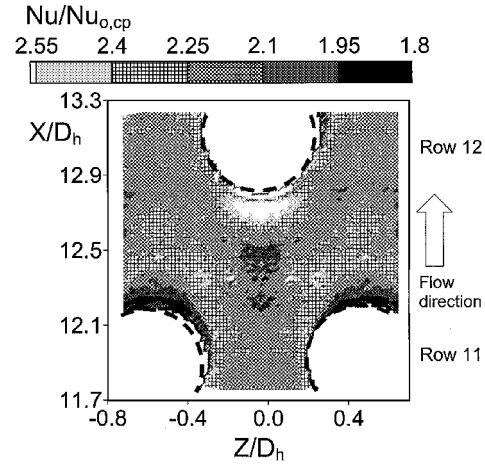

Fig. 5 Time-averaged local Nusselt number ratio $Nu/Nu_{0,cp}$ distribution along the bottom pin-fin test surface for $Re_H = 1.83 \times 10^4$ and $T_{0i}/T_w = 0.93$.

B. Spatially Resolved Distributions of Local Nusselt Numbers

Figure 5 presents spatially resolved Nusselt number ratios $Nu/Nu_{0,cp}$, measured over about one period of pin-fin surface pattern, on the bottom test surface. The white circular regions encircled by the dotted lines represent the locations of the pin bases. The results are given for $Re_H = 1.8 \times 10^4$ and $T_{0i}/T_w = 0.93$ and are obtained over a measurement area near the downstream portion of the test surface that extends over X/D_h from 11.7 to 13.3. This is in the vicinity of pins in the 11th and 12th rows. In Fig. 5, flow is directed from bottom to top in the increasing X/D_h direction. The data in Fig. 5 and the ones that follow are time-averaged using 25 instantaneous data sets acquired over a period of 25 s.

$Nu/Nu_{0,cp}$ variations on the bottom surface in Fig. 5 show a number of features that are due to different flow structures that develop because of the presence of the pin fins. One of these is a wake, which forms behind each pin fin. Even though mixing is enhanced, local $Nu/Nu_{0,cp}$ are relatively low in the wake region just downstream of the pin fins because of a flow recirculation zone and relatively low flow velocities. Farther downstream, local $Nu/Nu_{0,cp}$ values increase to become greater than 2.25 as local flow velocities increase, and large-scale unsteadiness forms (with length scales approximately equal to d). These high $Nu/Nu_{0,cp}$ regions are evident in Fig. 5 at Z/D_h values less than -0.3 and at Z/D_h values greater than $+0.3$ and at X/D_h values from 12.3 to 12.7. At the edges of the wakes, a shear layer is present where the low-speed wake flow interfaces with higher-speed flow away from the pin fins. Because of the high shear, turbulence production and transport are enhanced, along with local surface Nusselt numbers. The associated augmented $Nu/Nu_{0,cp}$ in Fig. 5 are then located along vertical strips over X/D_h from 11.8 to 12.7 that emanate from the spanwise edges of the pins near Z/D_h of -0.25 and $+0.25$. A third mechanism for local heat transfer enhancement is the horseshoe vortices that form upstream of each pin fin at the pin-wall junction. The enhancement is a result of the secondary advection provided by these vortices as they advect away from the stagnation line located on the upstream pin-fin edge. The secondary advection rearranges cooler fluid, originally located from away from the test surface, so that it is in close proximity with the heated test surface. One example of the resulting Nu/Nu_0 enhancement is evident in Fig. 5 at Z/D_h from -0.3 to $+0.3$ and at X/D_h from 12.6 to 12.8.

The effects of temperature ratio T_{0i}/T_w and variable properties on spatial distributions of $Nu/Nu_{0,cp}$ are illustrated by the results presented in Fig. 6. For the results presented in Fig. 6, Reynolds number Re_H is 2.14×10^4 and T_{0i}/T_w is 0.86. Because the Reynolds number variation from Fig. 5 to 6 is relatively small, it has almost no effect in altering local Nusselt numbers. The observed Nusselt number changes are instead due to different T_{0i}/T_w values. The results in Fig. 6 are measured at the same locations on the bottom surface as the results presented in Fig. 5. The white circular regions enclosed

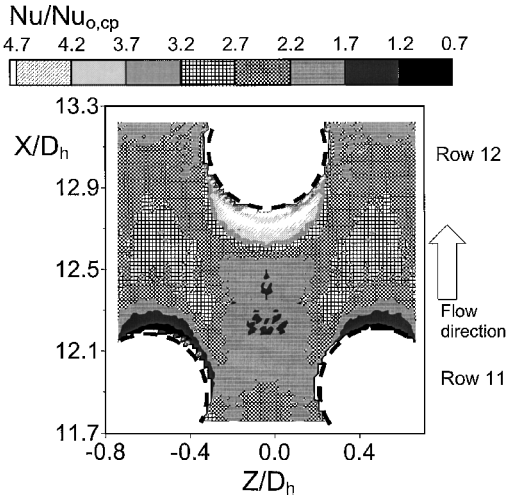

Fig. 6 Time-averaged local Nusselt number ratio $Nu/Nu_{0,cp}$ distribution along the bottom pin-fin test surface for $Re_H = 2.14 \times 10^4$ and $T_{0i}/T_w = 0.86$.

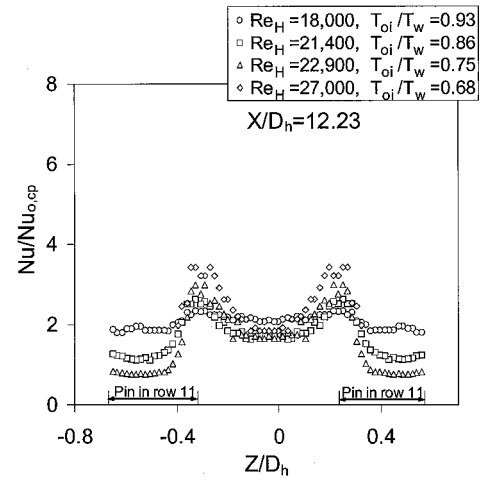

Fig. 7 Local Nusselt number ratios $Nu/Nu_{0,cp}$ as they vary in the normalized spanwise direction at $X/D_h = 12.23$ for different temperature ratios T_{0i}/T_w.

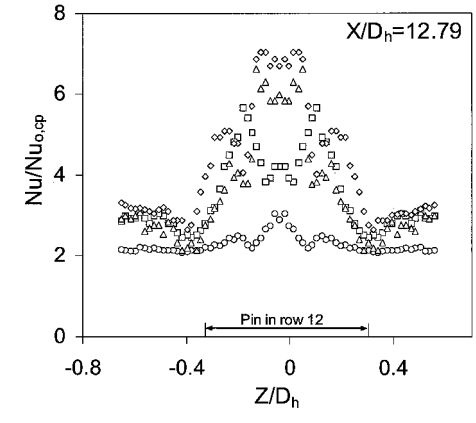

Fig. 8 Local Nusselt number ratios $Nu/Nu_{0,cp}$ as they vary in the normalized spanwise direction at $X/D_h = 12.79$ for different temperature ratios T_{0i}/T_w (symbols are defined in Fig. 7).

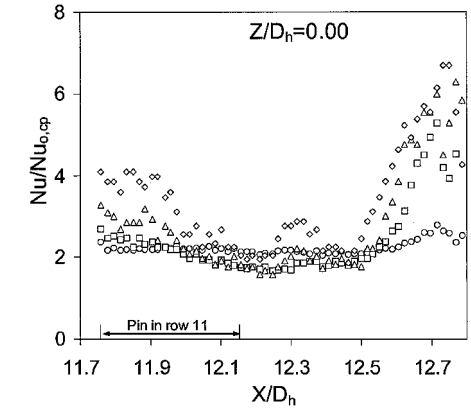

Fig. 9 Local Nusselt number ratios $Nu/Nu_{0,cp}$ as they vary in the normalized streamwise direction at $Z/D_h = 0.0$ for different temperature ratios T_{0i}/T_w (symbols are defined in Fig. 7).

by the dotted lines again denote the regions where the pin bases are located, as mentioned earlier. Note that different scales are used to plot the results in Figs. 5 and 6. This approach is employed to show variations that result from different flow features and because overall $Nu/Nu_{0,cp}$ changes in Fig. 5 are smaller than the variations in Fig. 6.

When compared to the results in Fig. 5, the $Nu/Nu_{0,cp}$ distribution in Fig. 6 increases significantly at several locations on the test surface as the temperature ratio decreases. These include the wake regions downstream of the pins in row 11 and the peripheral regions just upstream of pins in the 12th row. The region with increased $Nu/Nu_{0,cp}$ values located just upstream of the pins in row 12 also expands in both the upstream and downstream directions as T_{0i}/T_w decreases. The is due to the action of the horseshoe vortices and associated secondary flows as they advect cooler fluid from the bulk stream toward the wall and warmer fluid from the wall over a range of length scales. Nusselt number ratios between the adjacent pins outside the wake regions change only slightly with T_{0i}/T_w. The only locations where $Nu/Nu_{0,cp}$ values decrease (as T_{0i}/T_w decreases) are located immediately downstream of the pins in the 11th streamwise row, where flow separation and recirculation effects are strong.

The $Nu/Nu_{0,cp}$ variations with X/D_h in Figs. 5 and 6 are for fully developed flow in the pin-fin array. As a result, the thermal and fluid flowfields are approximately periodic with X/D_h as the pin fin placement pattern repeats itself. In many cases, this periodicity is accompanied by slight decreases of local $Nu/Nu_{0,cp}$ values with X/D_h for each successive $Nu/Nu_{0,cp}$ pattern. The periodicity that accompanies fully developed flow is confirmed by the results in Figs. 5 and 6 and by other measurements made at discrete thermocouple locations upstream of the regions where these results are measured.

The effects of temperature ratio and variable properties on local Nusselt numbers are further illustrated by the results presented in Figs. 7–9. The data are obtained from the results such as the ones presented in Figs. 5 and 6 and are obtained either along lines of constant X/D_h or along lines of constant Z/D_h. As is the case for the data in Figs. 5 and 6, variations with Reynolds number Re_H are so small in Figs. 7–9 that they can be neglected relative to variations with temperature ratio, which ranges from 0.93 to 0.68 for these data. Note that no data from the pin cylindrical surface or pin base are included in any of these distributions.

In Fig. 7, $Nu/Nu_{0,cp}$ distributions are shown as they vary in the normalized spanwise direction along a line of constant X/D_h equal to 12.23. This X/D_h location corresponds to the streamwise location just downstream of the pins in row 11. $Nu/Nu_{0,cp}$ peaks are apparent in each distribution in Fig. 7, with local maxima positioned at Z/D_h of about -0.3 and $+0.3$. These are due to the shear layer that forms to the sides of the wake that develops downstream of each pin. As a result, $Nu/Nu_{0,cp}$ ratios at these flat surface locations increase significantly as T_{0i}/T_w decreases. The opposite Nusselt number ratio trend with temperature ratio is evident for $Z/D_h < -0.4$ and $Z/D_h > +0.4$. This is because of the flow recirculation zone just downstream of the pins in row 11 mentioned earlier. Only small $Nu/Nu_{0,cp}$ variations with T_{0i}/T_w are then evident on the flat surface between the wake shear layers at Z/D_h from -0.1 to $+0.1$.

The $Nu/Nu_{0,cp}$ distributions in Fig. 8 are given along a line of constant X/D_h equal to 12.79. This X/D_h value is located just

upstream of the pins in row 12. The high Nusselt number ratio region, positioned at Z/D_h from -0.3 to $+0.3$, is due to the horseshoe vortex that forms upstream of each pin fin. Here the dramatic $Nu/Nu_{0,\mathrm{cp}}$ increases with decreasing temperature ratio illustrate the power of vortices in augmenting turbulent transport by promoting fluid mixing over a range of length scales. Also influencing heat transfer on this part of the test surface are the shear layers on the sides of the wake from pins in the row immediately upstream. Another interesting feature of the data in Fig. 8 is the slight drop of local $Nu/Nu_{0,\mathrm{cp}}$ magnitudes (relative to adjacent values at each value of T_{0i}/T_w), which is evident near $Z/D_h = 0$ at the central part of each high Nusselt number augmentation region. Away from the parts of the surface affected by the horseshoe vortex and shear layers ($Z/D_h < -0.3$ and $Z/D_h > +0.3$), $Nu/Nu_{0,\mathrm{cp}}$ magnitudes are about constant with Z/D_h for each value of T_{0i}/T_w.

The remarkable Nusselt number ratio increase with decreasing temperature ratio, produced by the horseshoe vortices, is also illustrated by the results presented in Fig. 9. These data are obtained along a line of constant Z/D_h equal to 0.0. Here, the significant Nusselt number augmentations (from the horseshoe vortices) begin at X/D_h near 12.5 and continue at higher X/D_h values. A region with increasing $Nu/Nu_{0,\mathrm{cp}}$ (as T_{0i}/T_w decreases) is also located farther upstream at $X/D_h < 12$. This is due to the wakes that form downstream of the pins in the 10th row. Other local increases are apparent near X/D_h of 12.3. These are believed to be due to local increases of turbulence transport levels caused by flow convergence and merging of the boundary layers that are caused by the blockage produced by pin fins located upstream. Here, corresponding local $Nu/Nu_{0,\mathrm{cp}}$ increases are especially apparent for $T_{0i}/T_w = 0.68$, but are also evident for T_{0i}/T_w values of 0.75 and 0.86.

C. Spatially Averaged Nusselt Numbers

Spanwise-averaged and streamwise-averaged Nusselt number ratios, measured on the bottom surface of the test section, are presented in Figs. 10 and 11, respectively. These data are obtained by computing averages over one complete period of pin-fin surface geometry using spatially resolved $Nu/Nu_{0,\mathrm{cp}}$ distributions, such as the ones shown in Figs. 5 and 6. The square surface area (used to compute the averages) is positioned such that one edge and two corners are located at the centers of three pin fins located in rows 11 and 12. No data from the pin-fin cylindrical surfaces, or from the parts of the test surface beneath the pin-fin bases, are included as the spanwise and streamwise averages are determined. For these data, the temperature ratio T_{0i}/T_w varies between 0.68 and 0.93, whereas Reynolds number changes are relatively small (as for the data in Figs. 5–9).

The spanwise-averaged $\overline{Nu}/Nu_{0,\mathrm{cp}}$ data in Fig. 10 generally increase as X/D_h increases (up to a value of about 12.7) for each value of temperature ratio T_{0i}/T_w. The local maxima near $X/D_h = 12.3$ are due to the shear layers and wakes behind pins in the 11th row. The local maxima near $X/D_h = 12.7$ are due to the high local Nusselt numbers produced by the horseshoe vortices, which are positioned near the upstream edges of pin fins in the 12th row. The subsequent decrease of $\overline{Nu}/Nu_{0,\mathrm{cp}}$ values (at larger X/D_h locations) are due to relatively low local Nusselt numbers between pin fins in the 12th row. When all of the results in Fig. 10 are considered, it is evident that variations of spanwise-averaged Nusselt number ratios with X/D_h become much larger as the temperature ratio T_{0i}/T_w decreases.

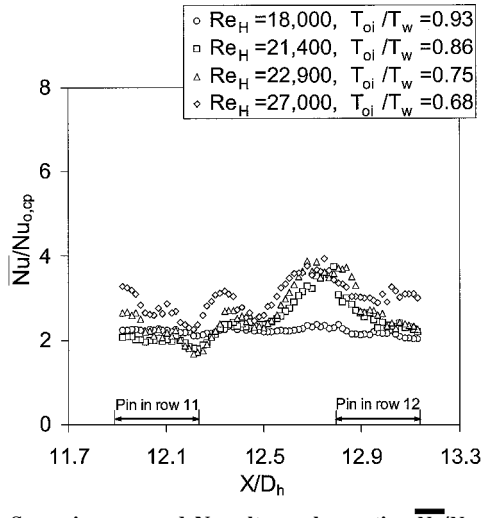

Fig. 10 Spanwise-averaged Nusselt number ratios $\overline{Nu}/Nu_0$ as they vary in the normalized streamwise direction for different temperature ratios T_{0i}/T_w.

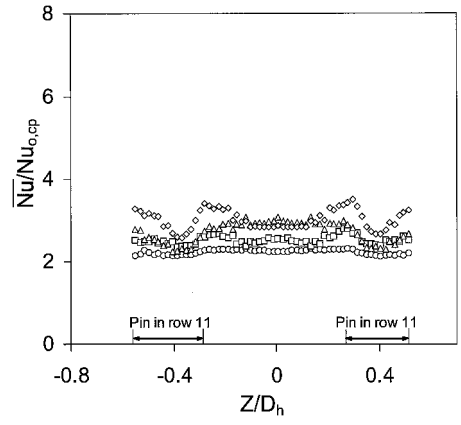

Fig. 11 Streamwise-averaged Nusselt number ratios $\overline{Nu}/Nu_0$ as they vary in the normalized spanwise direction for different temperature ratios T_{0i}/T_w (symbols are defined in Fig. 10).

A similar conclusion is reached after examination of the streamwise-averaged $\overline{Nu}/Nu_{0,\mathrm{cp}}$ data in Fig. 11. Here, the magnitudes of this ratio also generally increase at each location as T_{0i}/T_w decreases, just like the data in Fig. 10. A peak–trough–peak variation is especially apparent for lower temperature ratios at both $Z/D_h > 0.25$ and $Z/D_h < -0.25$. These are mostly due to the two shear layers and wake that are present downstream of each pin fin in the 11th row.

D. Globally Averaged Nusselt Numbers and Friction Factors

Globally averaged Nusselt numbers $\overline{Nu}$ are also determined from averages of local data over one complete period of pin-fin bottom surface geometry. As mentioned earlier, this is a square area that has one edge and two corners through the centers of three pin fins located in the 11th and 12th rows. Globally averaged friction factors are determined from wall static pressure drop measurements (at the same time as the Nusselt numbers are measured) along the portion of the test section where the flow is fully developed. For all presentations of these data, the variable property Nusselt number and variable property faction factor values are normalized. In Figs. 12 and 13, constant-property baseline values are employed for normalization to give $\overline{Nu}/Nu_{0,\mathrm{cp}}$ and $f/f_{0,\mathrm{cp}}$, respectively. In Figs. 14 and 15, constant-property pin-fin measured values are employed for normalization to give $\overline{Nu}/\overline{Nu}_{\mathrm{cp}}$ and f/f_{cp}, respectively. In all four cases, the ratios are presented as they are dependent on the temperature ratio T_{0i}/T_w as it varies from 0.68 to 0.93, for nearly constant Reynolds number Re_H.

Magnitudes of the present globally averaged $\overline{Nu}/Nu_{0,\mathrm{cp}}$ pin-fin data in Figs. 12, 14, and 16 are determined from measurements on the bottom test surface that exclude the pin-fin base area and from measurements on the bottom test surface that include heat transfer from the pin fins in rows 11 and 12. These latter values are determined from spatial averages of local Nusselt numbers measured on the flat base area of the test surface, and from spatial averages of local Nusselt numbers on the external surfaces of the pin fins. Nusselt number values along the length of each pin fin are determined from values measured around the periphery of each pin base, as suggested by Van Fossen[5] and Brigham and Van Fossen.[6] Note that the external surface of one-half of one pin comprises 33% of the total heat transfer surface area, and one complete period of flat bottom test surface geometry comprises 67% of the total heat

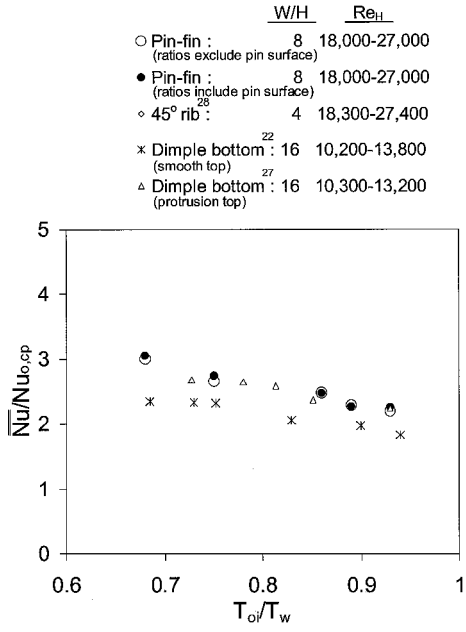

Fig. 12 Globally averaged Nusselt number ratios $\overline{Nu}/Nu_{0,cp}$ for fully developed flow conditions as dependent on T_{0i}/T_w; also included are results for other heat transfer augmentation devices.[22,27]

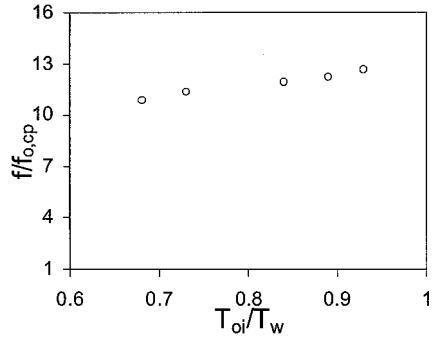

Fig. 13 Globally averaged friction factor ratios $f/f_{0,cp}$ for fully developed flow conditions as dependent on T_{0i}/T_w.

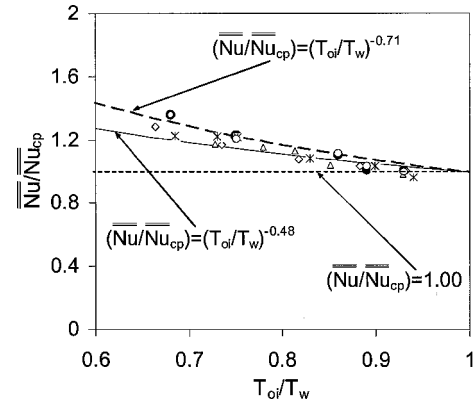

Fig. 14 Ratios of variable-property (globally averaged) pin-fin surface Nusselt numbers to constant-property (globally averaged) pin-fin surface Nusselt numbers $\overline{Nu}/\overline{Nu}_{cp}$, as dependent on the temperature ratio T_{0i}/T_w, for the present pin-fin channel and for other heat transfer augmentation devices[22,27,28] (symbols are defined in Fig. 12).

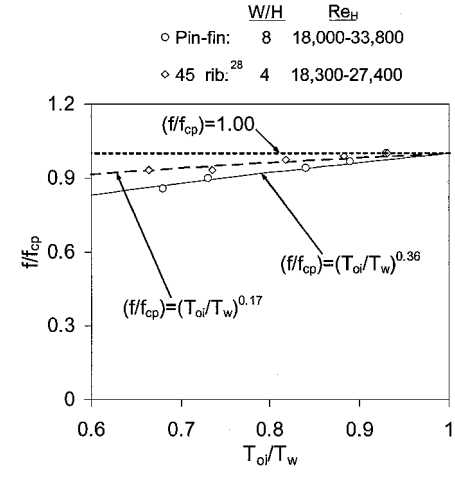

Fig. 15 Ratios of variable-property, pin-fin channel friction factors to constant-property pin-fin channel friction factors f/f_{cp}, as dependent on temperature ratio T_{0i}/T_w, for the present pin-fin channel and for a channel with rib turbulators.[28]

transfer surface area for this analysis. Also note that the power conducted into the two bases of each pin fin is the same as the convective power transferred from the entire external surface of the same pin fin.

The data in Figs. 12 and 13 are normalized using constant-property, smooth channel values because this gives ratios that quantify magnitudes of augmentation relative to a channel with no pin fins. The present globally averaged Nusselt number ratios in Fig. 12 are compared to values from a channel with a dimpled bottom wall and a smooth top wall[22] and a channel with a dimpled bottom wall and a top wall with protrusions.[27] Note that the channel aspect ratio for these studies is 16, compared to 8 for the present study. However, in spite of these differences, each of the four data sets presented in Fig. 12 shows a continuous $\overline{Nu}/Nu_{0,cp}$ increase as T_{0i}/T_w decreases. The highest values of $\overline{Nu}/Nu_{0,cp}$ at each temperature ratio are produced by the present pin fin surface and by a channel with dimples and protrusions.[27] The data from these sources[22,27] are chosen for comparison because they are the only ones known to the authors that give results regarding the effects of temperature ratio and variable properties for internal cooling configurations.

Note that the variable-property correction for channels with gas heating and smooth surfaces, from Kays and Crawford,[21] gives a decrease of variable-property, baseline Nu_0 by about 18% (compared to constant-property values) as T_{0i}/T_w decreases from 0.93 to 0.68. Equation (1) and data in Fig. 4 from the present study give a similar result. If variable-property baseline Nusselt numbers (instead of one constant-property Nusselt number value) are used to normalize the Nusselt number data in Fig. 12, then the $\overline{Nu}/Nu_{0,cp}$ value for $T_{0i}/T_w = 0.66$ increases by an additional 18%.

In contrast to the data in Fig. 12, the variable property friction factor ratios in Fig. 13 (for the present pin-fin channel) decrease as T_{0i}/T_w decreases from 0.94 to 0.66 (and Re_H Reynolds number is approximately constant at 1.8×10^4 to 3.38×10^4). This means that the flow and thermal fields have different dependence on variable property/temperature ratio effects, which is consistent with Kays and Crawford.[21] The baseline, that is, smooth channel, constant-property friction factors $f_{0,cp}$ that are used for normalization here are determined at $T_{0i}/T_w = 0.93$ using the Kármán–Nikuradse correlation (see Ref. 21). Figure 13 also shows that the present globally averaged friction factor ratios are quite high. This is largely because of the large amounts of form drag imparted on the flow by the blockage provided by the pin-fin array. The blockage ratio (ratio of frontal projected area of pins or ribs to channel cross-sectional area) for the pin-fin channel is 3.5 times the blockage ratio present in the ribbed channel investigated by Mahmood and Ligrani.[28]

The data in Figs. 14 and 15 are normalized using constant-property pin-fin values because this gives ratios that show the effects of different temperature ratios and variable properties. The present globally averaged Nusselt number ratios in Fig. 14 are also compared to values from other channels with other types of heat transfer augmentation devices.[22,27,28] However, in spite of the differences between these devices, all five data sets presented in Fig. 14 show

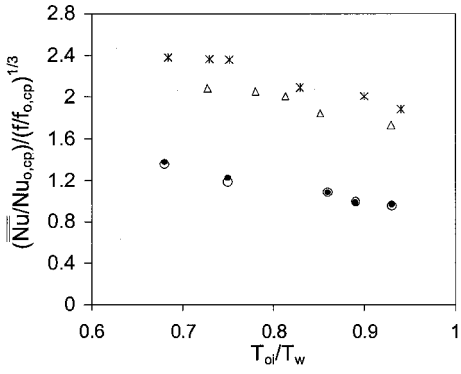

Fig. 16 Pin-fin channel thermal performance parameters as dependent on T_{0i}/T_w for Re_H from 1.8×10^4 to 2.74×10^4, including comparisons with thermal performance parameter magnitudes produced by other heat transfer augmentation devices[22,27] (symbols are defined in Fig. 12).

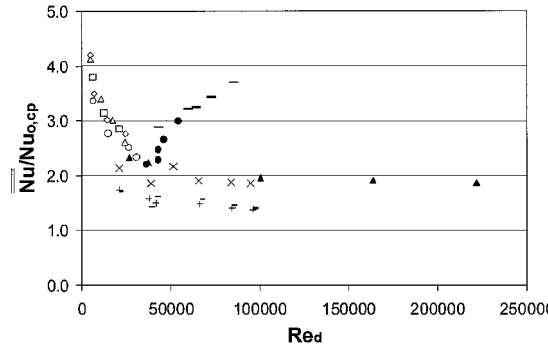

Fig. 17 Comparison of globally averaged Nusselt number ratios $\overline{Nu}/Nu_{0,cp}$ as dependent on Reynolds number Re_d to data from other pin-fin investigations: ○, circular, in-line;[10] △, circular, staggered;[10] □, fillet cylinder, in-line;[10] ◇, fillet cylinder, staggered;[10] ×, circular, staggered;[19] —, elliptic SEF, staggered;[19] +, elliptic N fin, staggered;[19] —, angled pedestals, staggered, varying T_{0i}/T_w (Ref. 14); ●, present study, including pin surfaces, varying T_{0i}/T_w; and ▲, present study, including pin surfaces, varying Re_H.

very similar dependence on temperature ratio T_{0i}/T_w. The present pin-fin data are well represented by an equation having the form

$$\overline{Nu}/\overline{Nu}_{cp} = (T_{0i}/T_w)^n \tag{2}$$

where $n = -0.71$ either when heat transfer from the pins is included or when heat transfer from the pin fins and pin-fin bases is excluded. According to Mahmood and Ligrani,[28] variable property rib turbulator data (as well as the data from the channels with protrusions and dimples[22,27]) are best represented using $n = -0.48$. The variations with T_{0i}/T_w, shown in Fig. 14, thus, indicate that heat transfer augmentations in channels with pin fins, rib turbulators, dimples, or protrusions all increase as the ratio of inlet stagnation temperature to local surface temperature decreases. The variable property method suggested by Olson[14] for a channel with pin fins employs $(T_w/T_f)^{0.55}$ (where T_f is the local bulk fluid temperature) and, thus, also gives this same overall trend.

The dependence of friction factor ratios f/f_{cp} on T_{0i}/T_w is shown in Fig. 15. These data are given for Reynolds numbers Re_H from 1.8×10^4 to 3.38×10^4 and for T_{0i}/T_w from 0.68 to 0.93. The present variable-property pin-fin data are well represented using an equation given by

$$f/f_{cp} = (T_{0i}/T_w)^n \tag{3}$$

where $n = 0.36$. This gives slightly greater temperature ratio dependence compared to the rib turbulator data,[28] which are also shown in Fig. 15, for which $n = 0.17$. The present pin-fin variable-property friction factor ratios also show greater dependence on T_{0i}/T_w than those given by the correlation from Kays and Crawford[21] for smooth ducts and no pin fins (also with gas flow heating).

E. Thermal Performance Parameters

The performance parameter, $(\overline{Nu}/Nu_{0,cp})/(f/f_{0,cp})^{1/3}$, given by Gee and Webb,[30] provides a measure of the amount of heat transfer augmentation relative to the pressure drop penalty, where each ratio is given for the same fluid pumping power. Figure 16 shows magnitudes of this performance parameter (as dependent on the temperature ratio T_{0i}/T_w) for the present pin-fin channel, along with values from a channel with a dimpled bottom wall and a smooth top wall[22] and a channel with a dimpled bottom wall and a top wall with protrusions.[27] The present data are obtained from the results presented in Figs. 12 and 13. Note that the present data are given for two arrangements of the bottom test surface: 1) excluding the pin-fin base area and 2) including heat transfer from the pin fins.

For each of these channel configurations, parameters increase as the temperature ratio T_{0i}/T_w decreases (and the Reynolds number is about constant) with a rate of increase that is roughly the same. This is a result of complex interactions between instantaneous secondary flows produced by the different devices and the local temperature gradients in the fluid. According to the data in Figs. 12, 14, and 16, these interactions result in near-wall, thermal turbulent transport levels that become larger as the overall temperature gradients and overall temperature differences in the channel increase.

When the pin-fin base area is excluded, the present test surface performance parameters range from 0.95 to about 1.36 as T_{0i}/T_w decreases from 0.93 to 0.68. When heat transfer from the pin fins is included, performance parameters from the present investigation range from 0.97 to 1.38 over the same range of T_{0i}/T_w values. Figure 16 shows that these values are lower than values measured at the same temperature ratios in channels with either dimples or protrusions.[22,27] This is mostly due to the higher flow blockage and higher friction factors produced by the pins, that are largely a result of the flow separation and reattachment zones that are located just downstream of each one. This is further substantiated by comparisons of these results with the data in Figs. 12–15, which reveal important differences between the pin-fin data and the data produced by the other devices.

F. Comparisons with Other Pin-Fin Investigations

In Fig. 17, results from the present study are compared to data from other pin fin investigations in $\overline{Nu}/Nu_{0,cp}$ vs Reynolds number Re_d coordinates. Included are data obtained from the present test facility, both as the Reynolds number Re_d varies and as the temperature ratio T_{0i}/T_w varies. This Reynolds number is based on pin-fin diameter d and the maximum velocity that exists at the location in the pin-fin array with the greatest blockage, where the cross-sectional area of the flow is minimum, as suggested by Chyu.[10] The Nusselt number data in Fig. 17 are plotted as dependent on this parameter because data from Chyu,[10] data from Uzol and Camci,[19] and the present Re_d varying data for circular-staggered pin fins collect in one continuous distribution. This not only illustrates the agreement and consistency of these three different sets of data, but also indicates the usefulness of this parameter in correlating heat transfer data from channels with pin fins. Circular-staggered pin-fin data from Refs. 10 and 19 and the present study are then in approximate agreement with values from Chyu[10] for circular-in-line, fillet-cylinder-in-line, and fillet-cylinder-staggered types of pin fins, but are higher than elliptic pin-fin data (N fin and SEF) from Uzol and Camci.[19]

Figure 17 also shows that $\overline{Nu}/Nu_{0,cp}$ data from the present study increase from 2.2 to 3.0 as the temperature ratio T_{0i}/T_w decreases from 0.93 to 0.68. Because of the effects of variable properties, these data are located above the circular-staggered pin-fin data obtained at different Reynolds numbers (and T_{0i}/T_w near 1.0). The staggered-pedestal data from Olson[14] show a similar trend because they are also obtained at T_{0i}/T_w values different from 1.0.

IV. Conclusions

Local Nusselt numbers, spatially averaged Nusselt numbers, globally averaged friction factors, and globally averaged thermal performance parameters (all time averaged) are presented for the bottom test surface of a pin-fin channel at different ratios of inlet stagnation temperature to local surface temperature T_{0i}/T_w. These

results provide information on the influences of variable properties of air for a situation where the gas is heated by the walls of the channel. The measurements are given for a channel aspect ratio of 8, temperature ratios from 0.68 to 0.93, and Reynolds numbers Re_H from 1.8×10^4 to 3.38×10^4. The pins are placed in 12 rows, with pin diameter and spacing between adjacent pins in both directions all equal to the channel height.

When considered at one particular value of T_{0i}/T_w, local Nusselt number ratios on the bottom surface are generally relatively high beneath the wake and shear layers that are present downstream of each pin and beneath the horseshoe vortex that forms just upstream of each pin. As the temperature ratio T_{0i}/T_w decreases, magnitudes of local Nusselt number ratios in these regions generally increase substantially. Lower Nusselt number ratios, with less T_{0i}/T_w dependence, are then present on the parts of the test surface that are beneath the flow that is located between these shear layers.

Because of these variations, globally averaged Nusselt number ratios also increase significantly as the temperature ratio T_{0i}/T_w decreases from 0.93 to 0.68. When pin-fin base areas are excluded and heat transfer from the surrounding bottom surface only is considered, this increase is about 35% (provided that Reynolds number Re_H is approximately constant and values are normalized by baseline constant-property Nusselt numbers to give $\overline{Nu}/Nu_{0,\mathrm{cp}}$). When heat transfer from the pin surfaces and the surrounding bottom surfaces are both considered, this increase is about the same. Friction factor ratios $f/f_{0,\mathrm{cp}}$ then show different dependence on this temperature ratio because they decrease somewhat as T_{0i}/T_w decreases from 0.93 to 0.68 (again with approximately constant Reynolds number Re_H). The dependence of these data on temperature ratio is given by Eqs. (2) and (3), respectively. The Reynolds number based on pin-fin diameter and on the mean velocity that exists at the location in the pin-fin array with minimum cross-sectional area appears to be a good correlating parameter for pin-fin Nusselt number data.

When compared to the globally averaged Nusselt number augmentations produced by other devices, the present pin-fin $\overline{Nu}/Nu_{0,\mathrm{cp}}$ ratios are higher than those produced by a channel with dimples and a smooth opposite surface, provided that the data are compared at the same T_{0i}/T_w. However, the present pin fins give lower thermal performance parameters as a result of the substantially higher flow blockage and friction factors. This means that using pin fins is advantageous when $\overline{Nu}/Nu_{0,\mathrm{cp}}$ values and heat transfer augmentations are considered alone and low friction factor magnitudes are not needed, or when geometry considerations require the use of pin fins, such as for trailing-edge cooling of turbine airfoils.

Acknowledgments

The work presented in this paper was sponsored by an Advanced Gas Turbine Research Program research subcontract sponsored by the U.S. Department of Energy–National Energy Technology Laboratory through a cooperative agreement with the South Carolina Institute for Energy Studies at Clemson University. J. C. Han of Texas A&M University provided insight regarding the pin fin concept and suggestions for pin fin geometry.

References

[1]Zukauskas, A., "Heat Transfer From Tubes In Cross Flow," *Advances in Heat Transfer*, Vol. 8, 1972, pp. 96–160.

[2]Sparrow, E. M., Ramsey, J. W., and Altemani, C. A. C., "Experiments on In-Line Pin Fin Arrays and Performance Comparisons with Staggered Array," *Journal of Heat Transfer*, Vol. 102, 1980, pp. 44–50.

[3]Metzger, D. E., and Haley, S. W., "Heat Transfer Experiments and Flow Visualization for Arrays of Short Pin-Fins," American Society of Mechanical Engineers, ASME Paper 82-GT-138, June 1982.

[4]Metzger, D. E., Barry, R. A., and Bronson, J. P., "Developing Heat Transfer in Rectangular Ducts with Staggered Arrays of Short Pin-Fins," *Journal of Heat Transfer*, Vol. 104, 1982, pp. 700–706.

[5]Van Fossen, G. J., "Heat-Transfer Coefficients for Staggered Arrays of Short Pin-Fins," *Journal of Engineering for Power*, Vol. 104, 1982, pp. 268–274.

[6]Brigham, A. W., and Van Fossen, G. J., "Length to Diameter Ratio and Row Number Effects in Short Pin Fin Heat Transfer," *Journal of Engineering for Gas Turbines and Power*, Vol. 106, No. 1, 1984, pp. 241–245.

[7]Simoneau, R. J., and Van Fossen, G. J., "Effects of Location in an Array on Heat Transfer to a Short Cylinder in Cross Flow," *Journal of Heat Transfer*, Vol. 106, 1984, pp. 42–48.

[8]Lau, S. C., Han, J. C., and Kim, Y. S., "Turbulent Heat Transfer and Friction in Pin Fin Channels with Lateral Flow Ejection," *Journal of Heat Transfer*, Vol. 111, 1989, pp. 51–58.

[9]McMillin, R. D., and Lau, S. C., "Effects of Trailing-Edge Ejection on Local Heat (Mass) Transfer in Pin Fin Cooling Channels in Turbine Blades," *Journal of Turbomachinery*, Vol. 116, No. 1, 1994, pp. 159–168.

[10]Chyu, M. K., "Heat Transfer and Pressure Drop for Short Pin-Fin Arrays with Pin-Endwall Fillet," *Journal of Heat Transfer*, Vol. 112, No. 4, 1990, pp. 926–932.

[11]Chyu, M. K., and Goldstein, R. J., "Influence of an Array of Wall-Mounted Cylinders on the Mass Transfer from a Flat Surface," *International Journal of Heat and Mass Transfer*, Vol. 34, No. 9, 1991, pp. 2175–2186.

[12]Chyu, M. K., Hsing, Y. C., Shih, T. I.-P., and Natarajan, V., "Heat Transfer Contributions of Pins and Endwall in Pin-Fin Arrays: Effects of Thermal Boundary Condition Modeling," *Journal of Turbomachinery*, Vol. 121, No. 2, 1999, pp. 257–263.

[13]Grannis, V. B., and Sparrow, E. M., "Numerical Simulation of Fluid Flow Through an Array of Diamond Shaped Pin Fins," *Numerical Heat Transfer*, Pt. A, Vol. 19, 1991, pp. 381–403.

[14]Olson, D. A., "Heat Transfer in Thin, Compact Heat Exchangers with Circular, Rectangular, or Pin-Fin Flow Passages," *Journal of Heat Transfer*, Vol. 114, No. 2, 1992, pp. 373–382.

[15]Goldstein, R. J., Jabbari, M. Y., and Chen, S. B., "Convective Mass Transfer and Pressure Loss Characteristics of Staggered Short Pin-Fin Arrays," *International Journal of Heat and Mass Transfer*, Vol. 37, 1994, pp. 149–160.

[16]Chyu, M. K., and Natarajan, V., "Heat Transfer on the Base Surface of Three-Dimensional Protruding Elements," *International Journal of Heat and Mass Transfer*, Vol. 39, No. 14, 1996, pp. 2925–2935.

[17]Chyu, M. K., Hsing, Y. C., and Natarajan, V., "Convective Heat Transfer of Cubic Fin Arrays in a Narrow Channel," *Journal of Turbomachinery*, Vol. 120, No. 2, 1998, pp. 362–367.

[18]Hwang, J. J., and Lu, C. C., "Lateral-Flow Effect on Endwall Heat Transfer and Pressure Drop in a Pin-Fin Trapezoidal Duct of Various Pin Shapes," American Society of Mechanical Engineers, ASME Paper 2000-GT-232, June 2000.

[19]Uzol, O., and Camci, C., "Elliptical Pin Fins as an Alternative to Circular Pin Fins for Gas Turbine Blade Cooling Applications, Part 1: Endwall Heat Transfer and Total Pressure Loss Characteristics," American Society of Mechanical Engineers, ASME Paper 2001-GT-180, June 2001.

[20]Uzol, O., and Camci, C., "Elliptical Pin Fins as an Alternative to Circular Pin Fins for Gas Turbine Blade Cooling Applications, Part 2: Wake Flow Field Measurements and Visualization Using Particle Image Velocimetry," American Society of Mechanical Engineers, ASME Paper 2001-GT-181, June 2001.

[21]Kays, W. M., and Crawford, M. E., *Convective Heat and Mass Transfer*, 3rd ed., McGraw–Hill, New York, 1993, pp. 249, 355–362.

[22]Mahmood, G. I., Hill, M. L., Nelson, D. L., Ligrani, P. M., Moon, H.-K., and Glezer, B., "Local Heat Transfer and Flow Structure on and Above a Dimpled Surface in a Channel," *Journal of Turbomachinery*, Vol. 123, No. 1, 2001, pp. 115–123.

[23]Sargent, S. R., Hedlund, C. R., and Ligrani, P. M., "An Infrared Thermography Imaging System for Convective Heat Transfer Measurements in Complex Flows," *Measurement Science and Technology*, Vol. 9, No. 12, 1998, pp. 1974–1981.

[24]Kline, S. J., and McClintock, F. A., "Describing Uncertainties in Single Sample Experiments," *Mechanical Engineering*, Vol. 75, 1953, pp. 3–8.

[25]Moffat, R. J., "Describing the Uncertainties in Experimental Results," *Experimental Thermal and Fluid Science*, Vol. 1, No. 1, 1988, pp. 3–17.

[26]Lienhard, J. H., *A Heat Transfer Textbook*, 2nd ed., Prentice–Hall, Englewood Cliffs, NJ, 1987, pp. 338–343.

[27]Mahmood, G. I., Sabbagh, M. Z., and Ligrani, P. M., "Heat Transfer in a Channel with Dimples and Protrusions on Opposite Walls," *Journal of Thermophysics and Heat Transfer*, Vol. 15, No. 3, 2001, pp. 275–283.

[28]Mahmood, G. I., and Ligrani, P. M., "Variable Property and Temperature Ratio Effects on Nusselt Numbers in a Rectangular Channel with 45° Angled Rib Turbulators," *Journal of Heat Transfer* (submitted for publication).

[29]Sleicher, C. A., and Rouse, M. W., "A Convenient Correlation for Heat Transfer to Constant and Variable Property Fluids in Turbulent Pipe Flow," *International Journal of Heat and Mass Transfer*, Vol. 18, 1975, pp. 677–683.

[30]Gee, D. L., and Webb, R. L., "Forced Convection Heat Transfer in Helically Rib-Roughened Tubes," *International Journal of Heat and Mass Transfer*, Vol. 23, 1980, pp. 1127–1136.